Advances in Geo-Energy Research

Vol. 19, No. 2, p. 101-117, 2026

Original article

Dynamic response and spalling of cemented tailings backfill under cyclic impact

Liyuan Liu[1,2], Yu Xiang[2], Tao Wang[1,3], Kai Liu[4], Wenchuan Liu[5], Baoxu Yan[6]

[1]*China-Zambia Belt and Road Joint Laboratory on Green and Safe Development of Mineral Resources, University of Science and Technology Beijing, Beijing 100083, P. R. China*

[2]*School of Resources and Safety Engineering, University of Science and Technology Beijing, Beijing 100083, P. R. China*

[3]*School of Future Cities, University of Science and Technology Beijing, Beijing 100083, P. R. China*

[4]*Department of Engineering Science, University of Oxford, Oxford OX1 3PJ, UK*

[5]*State Key Laboratory of Coal Mine Disaster Dynamics and Control, Chongqing University, Chongqing 400044, P. R. China*

[6]*College of Energy Engineering, Key Laboratory of Western Mine Exploitation and Hazard Prevention, Ministry of Education, Xi'an University of Science and Technology, Xi'an 710054, P. R. China*

Keywords:
Cemented tailings backfill
dynamic mechanical behavior
cyclic impact loading
strain-rate sensitivity
failure mechanisms

Cited as:
Liu, L., Xiang, Y., Wang, T., Liu, K., Liu, W., Yan, B. Dynamic response and spalling of cemented tailings backfill under cyclic impact. Advances in Geo-Energy Research, 2026, 19(2): 101-117.
https://doi.org/10.46690/ager.2026.02.01

Abstract:
Deep mining safety relies on the dynamic stability of cemented tailings backfill; however, its failure mechanisms in intricate loading scenarios are not yet well understood. This study utilized a split Hopkinson pressure bar apparatus to investigate the dynamic mechanical characteristics of this material, specifically contrasting its response under single and repeated impact loads. The results indicated that both compressive and tensile strengths exhibit a pronounced dependency on the strain rate. A significant contribution of this work is the identification of a unique spalling circumferential fracture pattern under cyclic impact loading for the first time, which stands in contrast to the axial splitting failure observed during single impacts. Numerical simulations further demonstrated that this unique failure mode arises from compression-induced plastic damage. Besides, while the energy absorption capacity exhibits strain-rate hardening, cyclic loading triggers a progressive degradation of energy dissipation efficiency. Compared to natural rocks, the backfill exhibits an enhanced peak stress under repeated impacts, particularly at lower loading rates. This research offers novel perspectives on the fracturing characteristics and rate-dependent behavior of cemented tailings backfill, contributing to the enhancement of safety protocols in deep mining engineering operations.

1. Introduction

Cemented tailings backfill (CTB) is employed extensively in underground metallic mines to ensure structural stability. However, with rising mining depth and scale, CTB is increasingly subjected to complex dynamic loading, with strain rates typically ranging from 10^{-1} and 10^{3} s^{-1}, such as blasting and machine excavation (Liu et al., 2020; Wang et al., 2022, 2025a; Liu et al., 2026). To ensure the integrity of backfill materials, it has been a critical challenge to understand the complex dynamic mechanical behavior and failure mechanisms under these medium-to-high strain rate perturbations (Chen et al., 2021; Wang et al., 2024a, 2025b; Liu et al., 2025b).

Extensive research has characterized the dynamic compressive behavior of CTB, revealing pronounced strain-rate sensitivity and energy dissipation patterns. For instance, it has been demonstrated through split Hopkinson pressure bar (SHPB) tests that the peak dynamic stress increases with high-

Yandy Scientific Press

*Corresponding author.
E-mail address: liuliyuan@ustb.edu.cn (L. Liu); m202320125@xs.ustb.edu.cn (Y. Xiang); tao.w@ustb.edu.cn (T. Wang); kai.liu@eng.ox.ac.uk (K. Liu); wc_liu@cqu.edu.cn (W. Liu); yanbaoxu@xust.edu.cn (B. Yan).

Received November 10, 2025; revised December 11, 2025; accepted January 4, 2026; available online January 9, 2026.

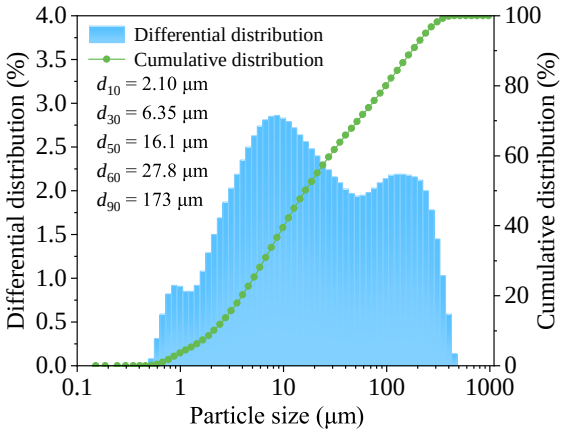

Fig. 1. Particle size distribution and cumulative gradation curve of tailings sand.

Table 1. Mineral composition and proportion of tailings sand (wt%).

Quartz	Potassium feldspar	Plagioclase feldspar	Calcite	Mica	Gypsum	Kaolinite
54.9	2.6	6.9	2.0	31.7	0.6	1.3

er cement-to-tailings ratios and impact velocities, while the dynamic strength enhancement factor escalates with the strain rate (Tan et al., 2019; Wang et al., 2024b). Similarly, dynamic strength exhibits a positive strain-rate dependence, often modeled by exponential functions, across various mixing ratios (Cao et al., 2018). Energy analyses indicated non-monotonic dissipation, with absorbed energy rising initially and then declining as strain rates increase (Zheng et al., 2021). Studies on layered CTB further showed that dynamic compressive strength and brittleness diminish with more layers and is influenced more by inclination angles than layer counts (Xue et al., 2021; Zhu et al., 2024). In related geomaterials and backfills, higher cementitious content enhances dynamic compressive strength within specific ranges, accompanied by aggregate grading effects that yield inconsistent strain-rate responses (Hou et al., 2023; Li et al., 2023; Xu et al., 2025a). These findings, derived from SHPB and similar high-strain-rate techniques, have advanced our understanding of material composition and structural influences on dynamic performance (Bischoff and Perry, 1991; Liu et al., 2019; Han et al., 2022; Qu et al., 2023).

Despite the above advances, two critical gaps have restricted the insights into CTB performance in underground mining environments where tensile and repetitive stresses are common. Systematic data and mechanisms of dynamic tensile behavior are relatively scarce, while static tensile properties, including constitutive relations and failure modes, have been explored under various conditions (Zhu et al., 2025; Zou et al., 2025b). Dynamic tensile strengths, strain-rate dependencies, failure initiation, and crack propagation under high-speed impacts remain poorly quantified, while they potentially lead to catastrophic structural failures. Besides, the damage accumulation, failure modes and strength evolution under cyclic impacts are unclear, although a preliminary study found that peak stress under cyclic loading can be double that of single impacts with reduced fracturing (Tan et al., 2020; Liu et al., 2024). The detailed processes of progressive energy dissipation and fracture patterns are underexplored, risking the underestimation of long-term stability in blasting scenarios. These gaps arise fundamentally from the limitations of experimental methods, such as inadequate designs for tensile and cyclic loading in conventional SHPB setups and insufficient mechanistic analyses.

To address the above limitations, this study employed a pendulum-based SHPB system to conduct systematic experiments on CTB, encompassing dynamic tensile tests, uniaxial compression tests, and cyclic impact tests. This approach enabled the comprehensive characterization of strain-rate dependencies, failure initiation, crack propagation, damage accumulation, and strength evolution under high-speed and cyclic loading conditions. Notably, a distinctive compressive plastic failure mode was identified for the first time in cyclic impact scenarios, revealing progressive energy dissipation trends and fracture patterns. Furthermore, Livermore Software Technology Corporation's Dynamic Analyzer (LS-DYNA) software was utilized to simulate the compressive plastic failure processes, providing mechanistic insights into the associated strength characteristics and non-homogeneous stress distributions. The findings of this study enhance the predictive modeling of CTB performance in underground mining environments, mitigating risks from tensile vulnerabilities and cyclic disturbances.

2. Experimental setup and method

2.1 Sample preparation

CTB specimens in this study were prepared using tailings sand, cement and water as raw materials. The tailings sand was sourced from a gold mine in Shandong Province, China. Its particle size distribution and gradation curve were measured using a Winner-2308 laser particle size analyzer. As shown in Fig. 1, the d_{10}, d_{30}, d_{60}, d_{90} values of this tailing sand are 2.10, 6.35, 27.8, and 173 μm, respectively, indicating that 10%, 30%, 60%, and 90% of the particles are smaller than these corresponding sizes. The inhomogeneity coefficient (C_u) and curvature coefficient (C_c) of the tailings sand were calculated as 3.024 and 0.691, respectively, indicating its relatively uniform but loosely graded characteristic. The mineral composition of tailings sand is shown in Table 1. To replace ordinary cement, one-part alkali-activated slag, an environmentally friendly homemade binder composed of more than 90 wt% industrial solid waste, was adopted. This binder comprised 67.83 wt% ground granulated blast furnace slag, 25.92 wt% desulfurization gypsum, and 6.25 wt% hydrated lime. More detailed physical and chemical information about one-part alkali-activated slag can be found in the literature (Zhu et al., 2022). Compared with ordinary Portland cement, this alternative binder produces less hydration heat and exhibits improved slurry fluidity within 20 h, which are advantageous for mining operations. The binder content was

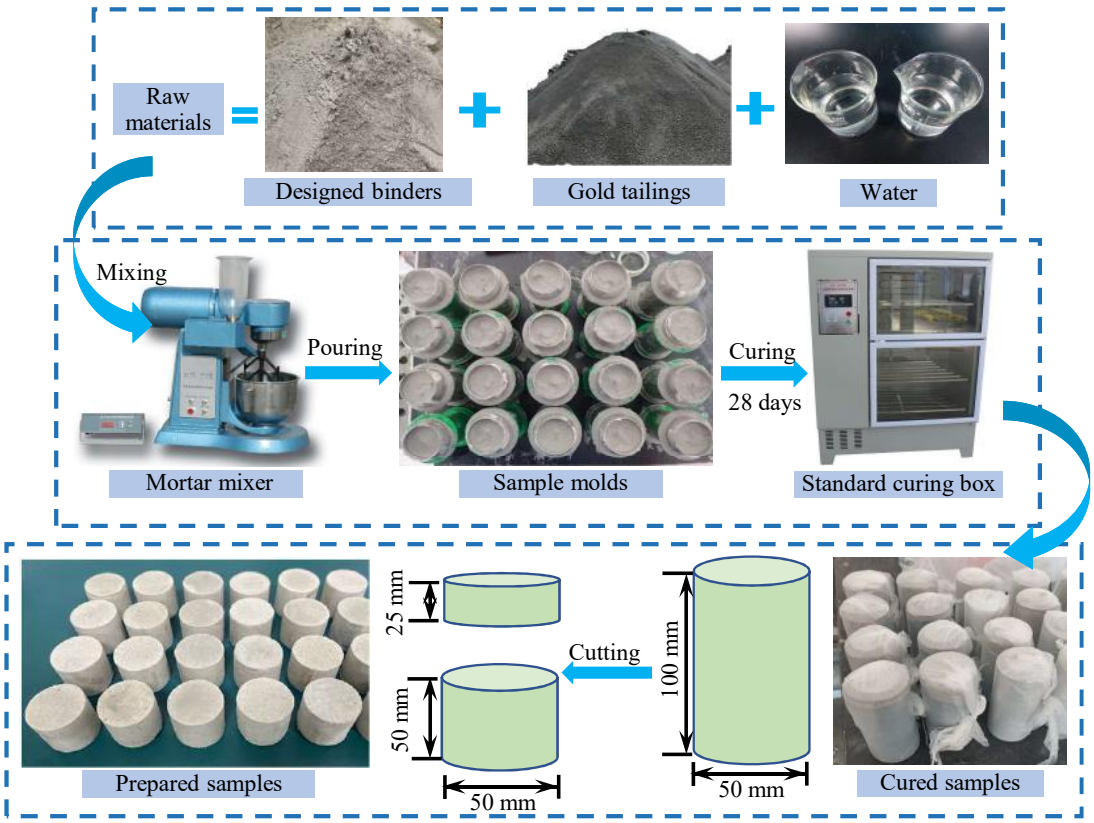

Fig. 2. Preparation and curing procedures of CTB specimens.

Table 2. Static physical and mechanical parameters of CTB specimens.

Density (kg/m^3)	UCS (MPa)	Elastic modulus (GPa)	Poisson's ratio (-)
2,036	4.103	0.741	0.18

established at 10% (corresponding to a cement-to-tailings mass ratio of 1:9), with the slurry mass concentration maintained at 73%, reflecting common field practices.

The specimen preparation procedure is presented in Fig. 2. The CTB materials were prepared according to the specified mix ratio, and water was added using a mechanical mixer to ensure uniform blending. The slurry was introduced into cylindrical molds with dimensions of 50 mm in diameter and 100 mm in height. Immediately after casting, the molds were placed in a curing chamber maintained at a temperature of 20 ± 2 °C and a humidity of $90\% \pm 5\%$ for 28 d. Uniaxial compressive static experiments were conducted on the hardened samples at a displacement rate of 0.05 mm/min, with the outcomes presented in Table 2.

Adhering to the procedures outlined by the International Society for Rock Mechanics, the samples were precisely shaped to meet standard specifications of 50 mm × 50 mm for cylindrical forms and 50 mm × 25 mm for disc-shaped ones. The end-face unevenness of the cylindrical specimens was required to be less than 0.01 mm, and that of the disc specimens to be less than 0.02 mm. The 50 mm × 50 mm cylindrical specimens were used for dynamic compression tests under single and cyclic impact loadings (i.e., dynamic uniaxial compression tests and cyclic impact tests), while the 50 mm × 25 mm disc specimens were used for dynamic Brazilian tensile tests. Although different specimen sizes were employed for tensile and compression tests, both specimen dimensions strictly adhered to the International Society for Rock Mechanics methodology and satisfied stress equilibrium conditions during testing. The results from both specimens were analyzed complementarily rather than comparatively. In this way, the influence of specimen size on test outcomes was negligible.

2.2 Testing apparatus

To investigate the effects of impact strain rate and the number of cyclic impacts on the dynamic properties and damage characteristics of CTB, a pendulum-style SHPB apparatus was utilized to carry out experiments at strain rates from moderate to elevated levels. As depicted in Fig. 3, the SHPB setup comprises a pendulum-powered loading assembly, an incident bar, a transmission bar, an energy absorber, and a data collection system. More detailed information can be found in the literature (Deng et al., 2025).

In this study, Brazilian tension tests, dynamic uniaxial compression tests and cyclic impact tests were performed on the prepared CTB specimens. All tests were conducted on the SHPB system using different loading methods, as illustrated in Fig. 3. Test data was recorded via strain gauges mounted

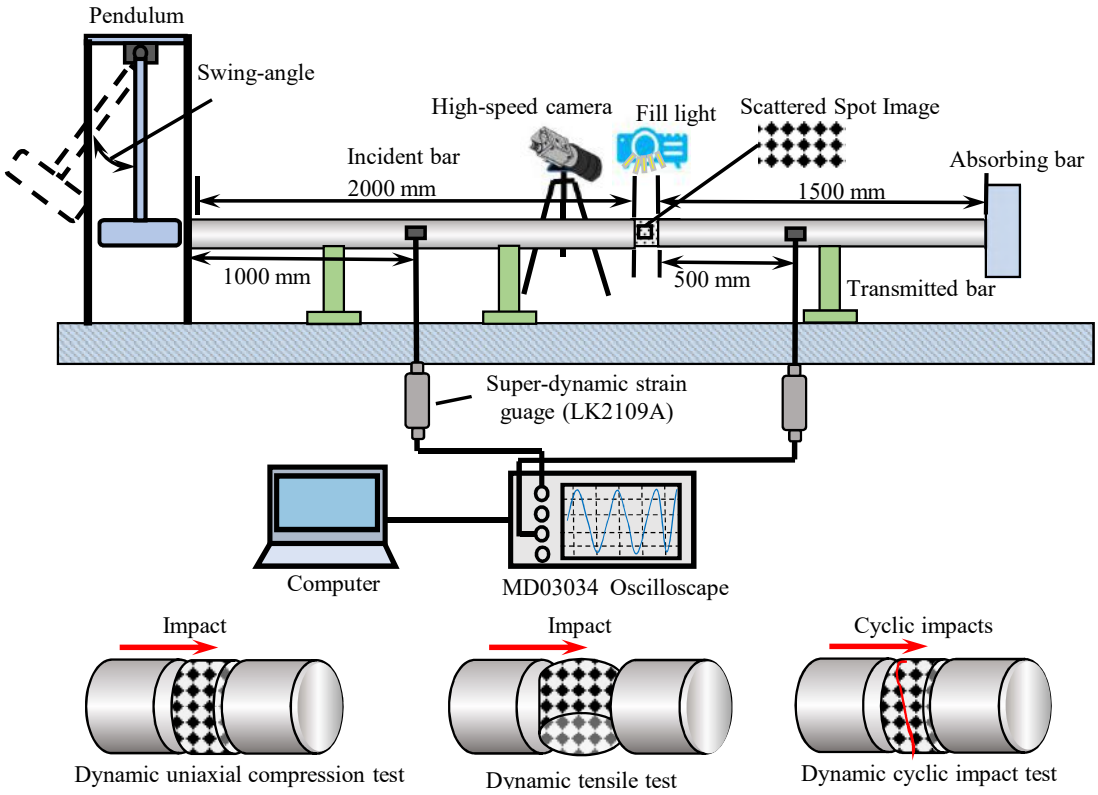

Fig. 3. Pendulum-type SHPB apparatus and loading configurations for CTB tests.

on the incident and transmission bar. Stress wave equilibrium was confirmed in all experiments. The mechanical behavior of the specimens under varying dynamic loading conditions was analyzed in terms of stress-strain response and failure morphology.

Throughout the experiments, speckle patterns were sprayed onto the specimen surfaces, while a high-speed charge coupled device camera was used in conjunction with digital image correlation (DIC) to record the complete deformation and fracture evolution across the entire field. The specific principle is to select the first image as the reference image, to compare the changes of the scattered spots on the subsequent images to obtain the small strains at that point, and finally to form the distribution of the strain field on the whole image. The camera was operated at a frame rate of 67,000 frames per second, corresponding to a temporal resolution of approximately 15 μs per frame. Given the inherent variability of high-speed impact tests, three specimens were tested independently under each set of experimental conditions to ensure repeatability and reduce statistical error.

Prior to the formal experiments, a series of preliminary experiments were conducted to select the pendulum angle. Specifically, minimum angle is defined as the angle at which the pendulum first causes specimen failure, with the corresponding impact velocity as the minimum speed. The test conditions were determined by increasing the impact velocity in incremental steps of 0.5 m/s. The testing matrix is presented in Table 3.

2.3 Data interpretation method

During the SHPB experiment, strain gauges affixed to the incident and transmission bars captured the profiles of incident, reflected, and transmitted strains. Based on one-dimensional elastic stress wave theory, the stress-strain response of the specimen is calculated after stress equilibrium is achieved (Kolsky, 1949; Lifshitz and Leber, 1994; Yao et al., 2017):

$$\sigma(t) = \frac{A_b E_b}{2A_s}\left[\varepsilon_i(t) + \varepsilon_r(t) + \varepsilon_t(t)\right] \tag{1}$$

$$\varepsilon(t) = \frac{C_b}{L_s}\int_0^t \left[\varepsilon_i(t) - \varepsilon_r(t) - \varepsilon_t(t)\right] \mathrm{d}t \tag{2}$$

$$\dot{\varepsilon}(t) = \frac{C_b}{L_s}\left[\varepsilon_i(t) - \varepsilon_r(t) - \varepsilon_t(t)\right] \tag{3}$$

where L_s denotes the length of specimens; t refers to time; $\sigma(t)$, $\varepsilon(t)$, and $\dot{\varepsilon}(t)$ represent the axial compressive stress, axial strain, and strain rate of the specimen, respectively; $\varepsilon_i(t)$, $\varepsilon_r(t)$, and $\varepsilon_t(t)$ denote the strain histories of incident, reflected wave, and transmitted wave, respectively. The cross-sectional area A, elastic modulus E, length L, and P-wave speed C_b are specified prior to data interpretation. Subscripts "b" and "s" refer to the bar and specimen, respectively.

Similarly, for the Brazilian tensile specimen, the dynamic forces $P_1(t)$ and $P_2(t)$ acting along the axial direction at the ends of the specimen can be calculated as: (Kolsky, 1963; Bieniawski and Hawkes, 1978):

$$P_1(t) = A_b E_b\left[\varepsilon_i(t) + \varepsilon_r(t)\right] \tag{4}$$

$$P_2(t) = A_b E_b \varepsilon_i(t) \tag{5}$$

Table 3. Experimental matrix for SHPB compression, cyclic impact, and Brazilian tensile tests.

Type	Sample size (mm^2)	Number	Pendulum angle (°)	Number of cycles
Dynamic uniaxial compression tests	Cylinder: 50×50	A25	43	1
		A30	52	1
		A35	61	1
		A40	71	1
		A45	82	1
		A51	97	1
Cyclic impact tests	Cylinder: 50×50	C30/C35	52/61	1
		C30/C35	52/61	2
		C30/C35	52/61	3
		C30/C35	52/61	4
		C35	52/61	5
Brazilian tensile tests	Disk: 50×25	B20	43	1
		B25	52	1
		B30	61	1
		B35	71	1
		B40	82	1

where $P(t)$ denotes the time-dependent dynamic force profile applied to the bars during impact. Once stress equilibrium is achieved, e.g., $P_1(t) = P_2(t)$, the tensile stress at the center of the disc specimen can be obtained as follows (Cho et al., 2003; Liu et al., 2025a):

$$\sigma_T(t) = \frac{A_b E_b \left[\varepsilon_i(t) + \varepsilon_r(t) + \varepsilon_t(t)\right]}{2\pi dH} = \frac{A_b E_b \varepsilon_t(t)}{\pi dH} \tag{6}$$

where $\sigma_T(t)$ represents the tensile stress at the center of the specimen, d and H represent the diameter and thickness of the Brazilian disc specimen, respectively, and the rest of the symbols have the same meaning as those in the compression test. The tensile strength is defined as the maximum tensile stress attained at the point of specimen failure. The $\sigma_T(t)$ curve includes a nearly linear section, where the slope indicates the loading rate:

$$\dot{\sigma}(t) = \frac{\sigma_T(t)}{t} \tag{7}$$

Then, the tensile strain rate $\dot{\varepsilon}_T(t)$ can be calculated as:

$$\dot{\varepsilon}_T(t) = \frac{\dot{\sigma}(t)}{E_s} \tag{8}$$

where E_s denotes the elastic modulus of the specimen, and $\dot{\sigma}(t)$ is loading rate.

Furthermore, to quantify the influence of strain rate on the dynamic strength of the specimen, the dynamic increase factor (DIF) is calculated at various strain rates (Malik et al., 2018; Lin et al., 2020; Song et al., 2024):

$$\mathrm{DIF} = \frac{\sigma_d}{\sigma_s} \tag{9}$$

where σ_d and σ_s are the dynamic strength and quasi-static strength of the specimens, respectively.

The process of deformation and destruction of the CTB is accompanied by the storage, transfer and consumption of energy. The dissipative energy W_c of the CTB can be calculated according to Eq. (10):

$$W_c = W_i - W_r - W_t \tag{10}$$

where W_c represents the dissipative energy of the CTB; W_i, W_r, and W_t refer to the energy of the incident, reflected, and the transmitted waves, respectively, which can be determined by the following equation (Zou et al., 2025a):

$$W = A_b E_b C \int \varepsilon_s^2(t)\mathrm{d}t \tag{11}$$

where $\varepsilon_s(t)$ denotes the strain history in the bar of SHPB, which includes the incident bar, the reflected bar, and the transmitted bar.

3. Results

This section presents the results of CTB specimens under dynamic tensile testing, dynamic uniaxial compression testing, and cyclic impact testing. All test data were subjected to analytical treatment, verifying the equilibrium state of stress waves. The mechanical behavior of the specimens subjected to various dynamic loading conditions was characterized by analyzing stress-strain responses, DIC-derived strain field evolution, damage development, and the associated failure patterns. Notably, under cyclic loading, the fillers showed a unique spalling fracture pattern along with the phenomenon of strength enhancement.

3.1 Dynamic tensile behaviors of CTB

3.1.1 Stress balance check and force history

The tensile stress history on the center line of the specimens obtained from the dynamic Brazilian splitting test of the CTB under impact angle of 71 ° (strain rate of 38.08 s^{-1}) are presented in Fig. 4(a). This stress data was calculated from strain gauge data affixed to the bars and Eq. (6). Once the dynamic stress equilibrium was obtained, the historical curves of tensile stress under different strain rates could be calculated and presented in Fig. 4(b). Initially, the tensile stress increases gradually, followed by a sharp rise. Then, it transitions into a phase of approximately linear growth, culminating in specimen failure at time t_f, where the stress undergoes a precipitous drop. The peak tensile strength at failure was calculated as 0.503 MPa based on Eq. (7), corresponding to a loading rate of 35.513 GPa/s.

In this study, dynamic Brazilian splitting tests were conducted at five different impact angles. The corresponding parameters, including strain rate and peak tensile strength, were calculated using Eqs. (4)-(8) and are summarized in Table 4.

To compare the dynamic tensile stress characteristics of CTB under different strain rates, Fig. 4(b) presents the ten-

Table 4. Statistical table of experimental data under dynamic splitting action.

Impact angle (°)/Impact velocity (m/s)	Sample	Loading rate (GPa/s)	Strain rate (s^{-1})	Dynamic tensile peak stress (MPa)	Average tensile peak intensity (MPa)
34/2.0	B20-1	5.952	8.054	0.178	0.172
	B20-2	5.583	7.555	0.171	
	B20-3	5.236	7.085	0.166	
43/2.5	B25-1	18.923	25.606	0.279	0.278
	B25-2	19.356	26.192	0.284	
	B25-3	18.245	24.689	0.271	
52/3.0	B30-1	19.905	26.935	0.327	0.337
	B30-2	23.889	32.326	0.346	
	B30-3	21.123	28.583	0.339	
61/3.5	B35-1	25.237	34.150	0.412	0.410
	B35-2	24.368	32.974	0.401	
	B35-3	25.159	34.045	0.418	
71/4.0	B40-1	31.291	42.342	0.512	0.504
	B40-2	28.140	38.078	0.498	
	B40-3	32.513	43.996	0.503	

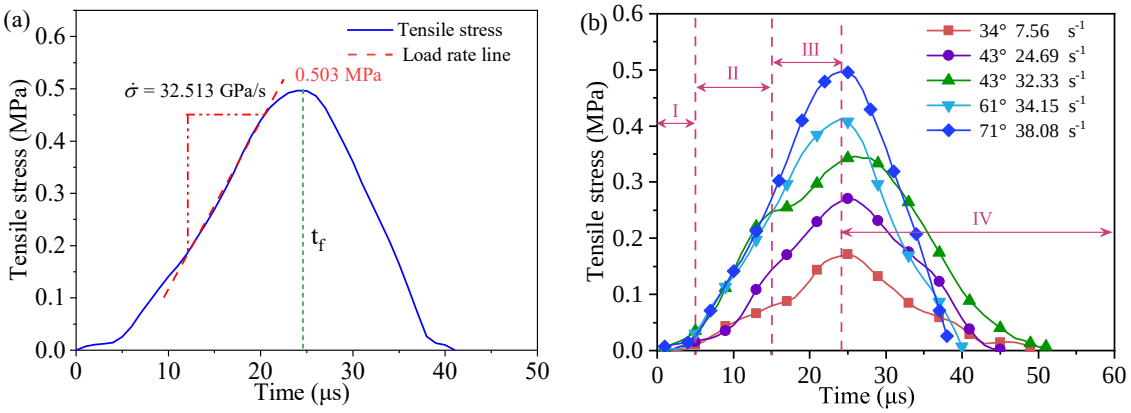

Fig. 4. Typical dynamic Brazilian tensile test curve of CTB: (a) Tensile stress evolution at the impact angle of 71° (strain rate of 38.08 s^{-1}) and (b) historical curves of tensile stress under different strain rates.

sile stress histories of CTB specimens subjected to different impact angles from 34° to 71°. The tensile stress history can be generally divided into four distinct stages: Stage I - compaction, Stage II - linear elasticity, Stage III - yielding, and Stage IV - failure. In Stage I, microcracks and pores within the CTB are compacted under high-velocity impact, resulting in nonlinear mechanical behavior. This is followed by Stage II, where the material exhibits an approximately linear elastic response. In Stage III, the accumulated elastic energy leads to stress concentration around inherent flaws, such as microcracks, which initiates their propagation. This process continues until the tensile stress reaches its peak, marking the ultimate tensile strength of CTB. The time required to reach peak stress does not significantly decrease. Meanwhile, in rock materials, the time required for the tensile stress curve to reach peak strength at high strain rates is significantly reduced (Feng et al., 2023). This difference may be attributed to the relatively lower tensile strength of the CTB. During Stage IV - failure, higher strain rates further increase the brittleness of CTB, speeding up the progression of damage.

3.1.2 Tensile failure patterns of CTB

Strain field images captured at different time points on the specimen surface aid in investigating the fracture mode of the

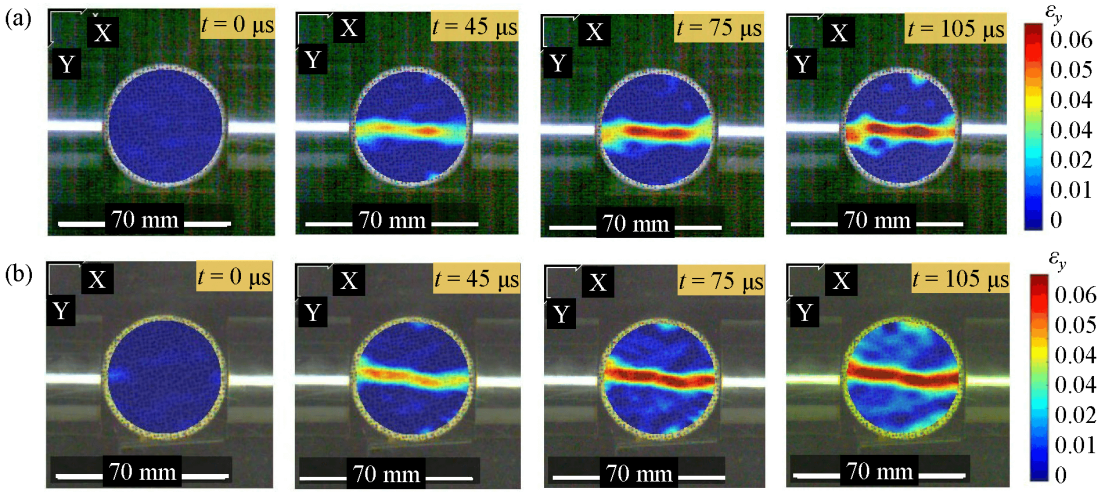

Fig. 5. IC strain field distributions of CTB Brazilian discs under dynamic impact loading: (a) 61° impact angle, 3.5 m/s and (b) 52° impact angle, 3.0 m/s.

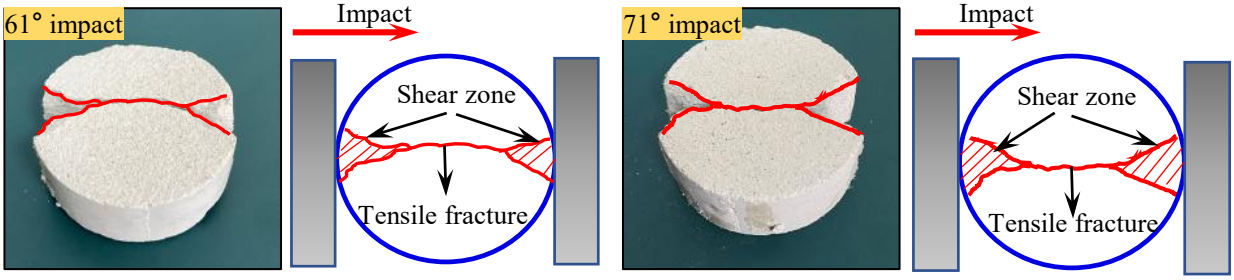

Fig. 6. Typical failure patterns of CTB specimens in dynamic Brazilian tensile tests at different impact angles.

specimen. Fig. 5 presents the dynamic tensile damage process of CTB specimens captured via DIC during Brazilian disc splitting tests at impact angles of 52° and 61°, with the impact velocity of 3.5 and 4.0 m/s, respectively. The DIC results successfully reproduce the primary failure process, confirming the accuracy of the Brazilian disc test under dynamic loading. As shown in Fig. 5(a), the crack first appears in the center of the specimen, then extends and develops from the middle to the two ends, which is a typical damage model of the Brazilian disk center initiation crack. The damage configuration is similar for both impact angles: A tensile crack develops parallel to the loading direction, while an axial crack propagates through the entire specimen, splitting it into two separate parts. As the impact angle (loading speed) increases, the tensile strain of the specimen increases and a branching crack develops, creating a shear damage zone at the two contact points of the disk.

In artificial CTB specimens, material heterogeneity leads to the initiation of primary tensile cracks that propagate roughly parallel to the impact direction, as illustrated in Fig. 6. These axial cracks partition specimens into two discrete segments, revealing two distinct failure modes: Tensile damage and shear damage. The tensile failure mechanism, an inherent characteristic of Brazilian disc testing, originates from the concentration of central tensile stress. Meanwhile, shear damage develops due to localized stress concentrations at specimen-loading rod interfaces, with shear zone dimensions demonstrating notable correlation with impact velocity.

3.2 Dynamic uniaxial compression behaviors of CTB

The results of dynamic unconfined compression tests, including strain rate, peak dynamic strength, average dynamic strength, and dynamic strength increase factor at various pendulum angles, were summarized in Table 5. The strain rates of specimens corresponding to impact angles from 43° to 97° range from 36.81 to 89.20 s^{-1}, falling within the intermediate-to-high strain rate regime.

3.2.1 Stress balance check, stress strain curves and strain rate effect

On the basis of the one-dimensional elastic wave theory, the validity of dynamic unconfined compression tests using the SHPB system relies on achieving dynamic stress equilibrium. As depicted in Fig. 7(a), the combined incident and reflected waves within the incident bar align closely with the transmitted wave in the transmission bar, verifying that the cylindrical CTB sample achieves uniform stress at both extremities. Meanwhile, dynamic loading in SHPB tests is typically characterized by strain rate, which is calculated using Eq. (3). The time history of the strain rate during loading is presented in Fig. 7(b). A plateau can be observed in the time window between t_0 and t_1, where t_0 denotes the moment the specimen reaches dynamic stress equilibrium, and t_1 corresponds to the onset of a strain rate jump. The dynamic strain rate is taken

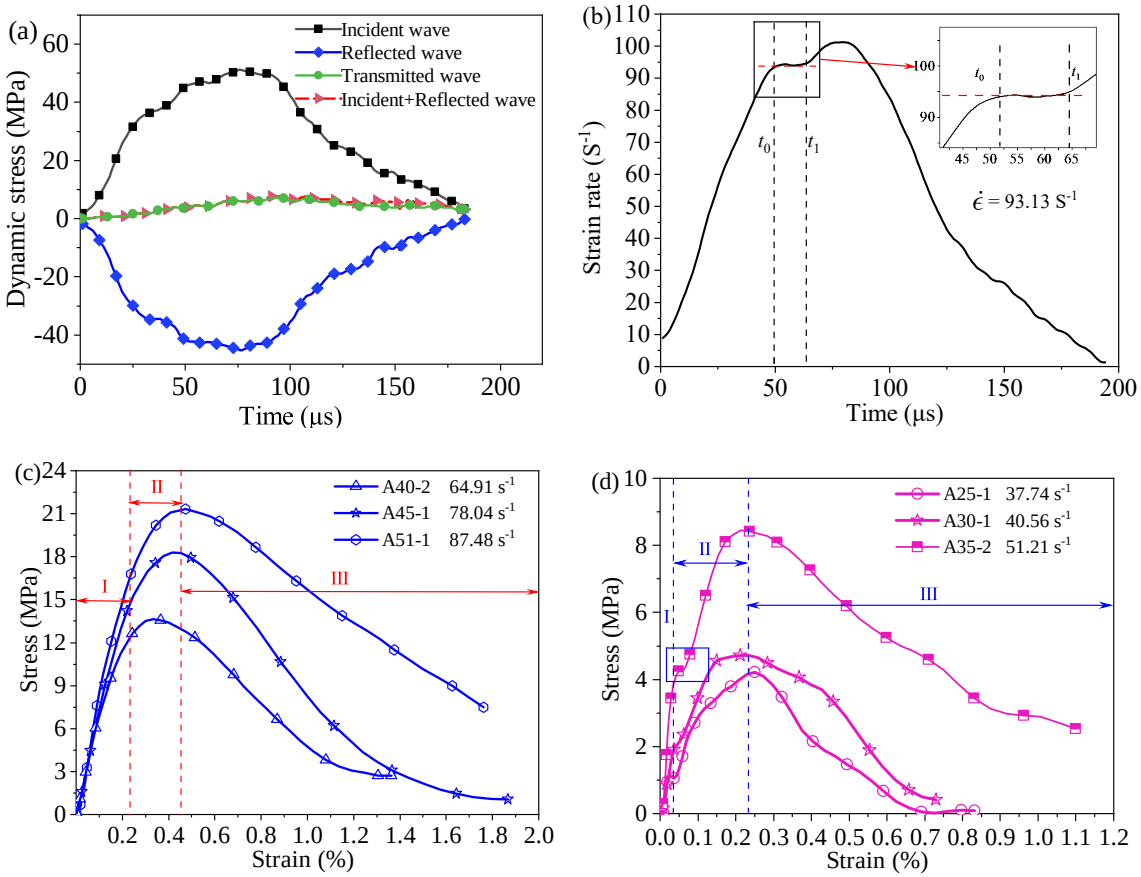

Fig. 7. Dynamic compression test results of CTB: (a) Stress equilibrium verification, (b) strain rate history at 97° impact angle, stress-strain curves at impact velocities of (c) 2.5-3.5 m/s, and (d) 4.0-5.1 m/s.

as the average value within this interval. For the specimen impacted with the velocity of 5.1 m/s, the average strain rate is calculated to be 93.13 s^{-1}, further confirming the validity of the dynamic compression test.

The dynamic stress-strain relationships of samples obtained at various strain rates are shown in Figs. 7(c) and 7(d). The results from the unconfined impact tests on the CTB indicate a pronounced strain-rate dependence, with the DIF attaining a peak value of 5.3, as summarized in Table 5. The stress-strain responses measured under six different impact angles can be partitioned into three stages: An elastic phase, a yield phase, and a post-peak damage phase. During the post-peak damage stage, the curves exhibit no elastic rebound and strain continues to accumulate, indicating substantial plastic behavior in the CTB specimens. Despite the presence of numerous internal pores within the backfill material (Zhao et al., 2023; Zhang et al., 2024b), the stress-strain curves under impact loading bypass the compaction stage and directly enter the elastic stage, where the dynamic stress-strain relationship approximates linear growth. Subsequently, the curves transition into the yield stage, flattening as they near the peak stress. With increasing impact angles, the dynamic peak strength of the specimens rises, ranging from 4.03 to 21.76 MPa. Post-peak, the specimens do not undergo crushing failure and maintain residual load-bearing capacity. During this phase, accumulated elastic strain energy is dissipated via internal defects and surface microcracks, resulting in further deformation without complete structural collapse. The data depicted in Table 5 suggests a discernible linear relationship between strain rate and dynamic compression strength.

3.2.2 Failure pattern and DIC analysis

The dynamic deformation and failure behavior of CTB specimens under impact angles of 82° are illustrated in Fig. 8. As observed in Fig. 8(a), micro-cracks oriented parallel to the impact direction progressively develop on the specimen surface. These cracks originate at the end in contact with the transmission bar and then propagate and coalesce toward the end attached to the incident bar, ultimately forming a network-like structure. Nevertheless, the specimen exhibits no significant overall failure. In Fig. 8(b), the vertically concentrated strain zone reflects the stress wave on the specimen surface, which repeatedly travels along the axial direction between the two ends of the specimen.

Three representative specimens were chosen for analysis and are shown in Fig. 9. In the specimen with an impact angle of 61°, the small area of spalling damage appears only at the end of the side surface, and the entire specimen is not obviously damaged. When the impact angle is 82°, the damage is mostly due to shear-tensile failure. The end of the

Table 5. Experimental data of CTB under dynamic uniaxial compression.

Impact angle (°)/Velocity (m/s)	Sample	Strain rate (s^{-1})	Dynamic peak stress (MPa)	Dynamic increasing factor (-)	Average peak stress (MPa)
43/2.5	A25-1	36.12	4.03	0.983	4.12
	A25-2	37.74	4.22	1.029	
	A25-3	36.81	4.12	1.005	
52/3.0	A30-1	40.56	4.73	1.154	4.71
	A30-2	40.17	4.69	1.143	
	A30-3	40.64	4.59	1.120	
61/3.5	A35-1	50.78	8.26	2.015	8.36
	A35-2	51.21	8.45	2.061	
71/4.0	A40-1	63.85	13.83	3.373	13.74
	A40-2	64.91	13.64	3.327	
82/4.5	A45-1	78.04	18.28	4.459	17.99
	A45-2	75.44	17.69	4.315	
97/5.1	A51-1	87.48	21.33	5.202	21.61
	A51-2	93.13	21.76	5.307	

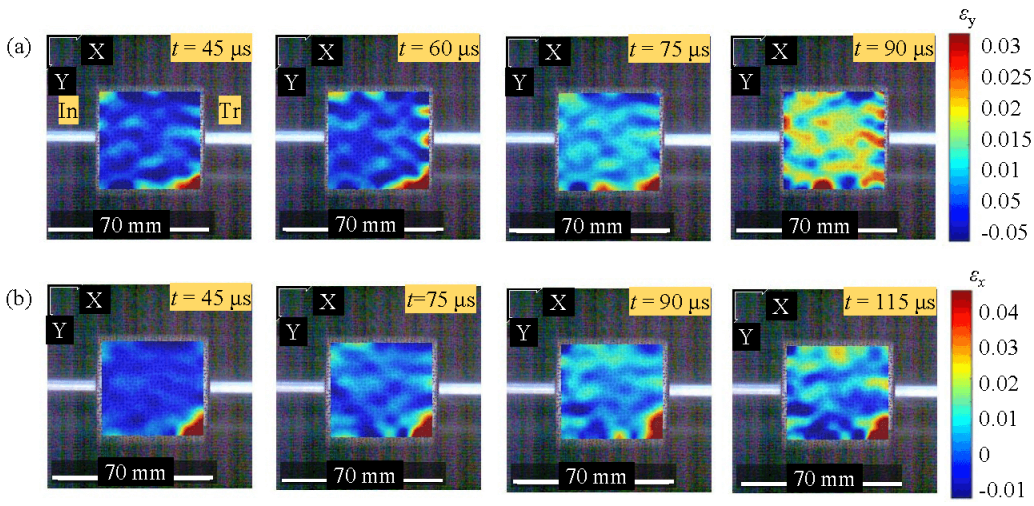

Fig. 8. DIC strain field distributions of CTB specimens under dynamic uniaxial impact loading at 4.5 m/s: (a) ε_y strain field and (b) ε_x strain field.

sample takes the worst hit, with cracks spreading axially from there, and secondary cracks forming to connect the main ones. Furthermore, as the impact angle increases, the sample starts flaking off in chunks, with the transmitted rod end showing even larger flaking areas.

Correlating Fig. 8 with Fig. 9, it is evident that the failure mode of CTB under dynamic uniaxial compression is characterized by splitting failure, predominantly marked by cracks parallel to the loading direction. Furthermore, due to the heterogeneity and multi-scale nature of the CTB material, the specimen initially experiences surface spalling while retaining a degree of internal structural integrity. This observation indicates that CTB maintains a residual load-bearing capacity following failure under dynamic loading, which is beneficial for ensuring the safe operation of mines.

3.3 Dynamic uniaxial cyclic behaviors for CTB

Drawing from the outcomes of the dynamic uniaxial compression experiments, two comparatively modest impact angles (52° and 61°) were chosen for cyclic dynamic loading to guarantee that the specimen could endure several impacts pr-

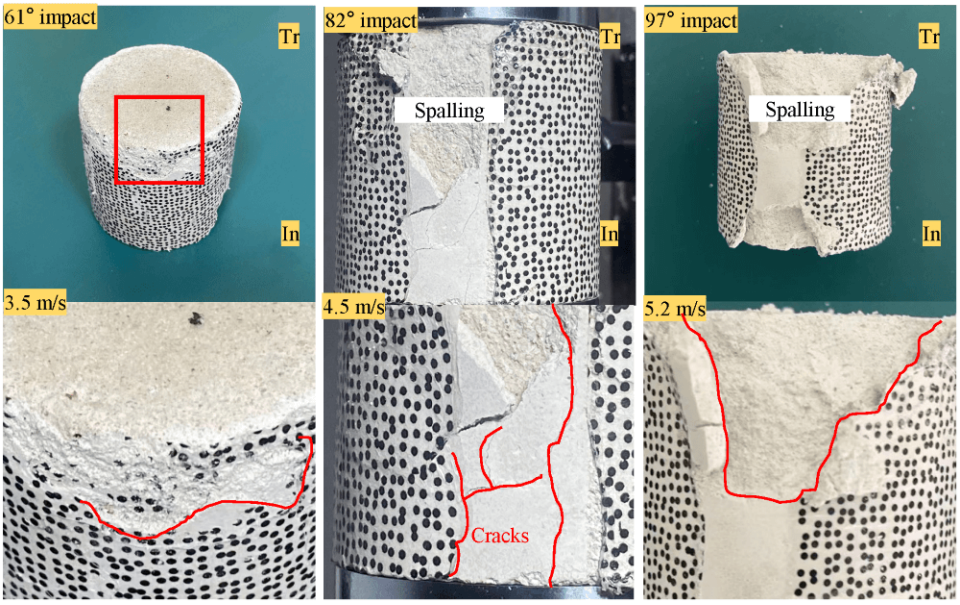

Fig. 9. Observed failure patterns of CTB specimens subjected to dynamic uniaxial impact loading.

Table 6. Statistical summary of CTB specimen responses under repeated dynamic impacts.

Impact angle (°)/velocity (m/s)	Sample	Strain rate (s^{-1})	Dynamic peak stress (MPa)
52/3.0	C30-1	42.62	4.53
	C30-2	41.48	5.17
	C30-3	39.42	6.34
	C30-4	38.48	6.90
	C30-5	44.52	7.66
61/3.5	C35-1	55.07	8.15
	C35-2	54.74	9.02
	C35-3	53.46	10.55
	C35-4	50.27	10.98

ior to complete failure. Cyclic loading was applied until the end faces of specimen became too uneven to maintain proper contact. A total of five and four loading cycles were conducted at 52° and 61°, respectively, with the corresponding test data presented in Table 6. While the strain rate remained relatively stable throughout the tests, it exhibited a slight overall decreasing trend due to the compaction of the specimen. Similarly, the dynamic compressive strength of the specimens showed a gradual increase as the number of impact cycles rose.

3.3.1 Stress-strain curves

The stress-strain curves for different cycle numbers at two impact angles are summarized in Fig. 10. All five curves at 52° impact angle are roughly observable for all three phases in the uniaxial impact test in Fig. 10(a). However, the stress-strain curve of the specimen shows a low stress peak before the peak stress is reached under 2-3 times of impact loading of the CTB. After the low stress wave peak, the stress continues to accumulate around the cracks that have been created, the cracks continue to develop, and the stress-strain curve keeps increasing beyond the peak and continues to rise until the specimen ultimately fails. As impact loading is continued, the phenomenon of low stress wave peak of the damaged specimen disappears, and the brittleness of the post-peak damage stage gradually increases. As shown in Fig. 10(b), the low-stress wave phenomenon does not appear at the 61° impact angle, which may be due to the fact that the increase of the impact angle leads to faster closure of the defects inside the specimen. All curves show a continuous increase in strain during the post-peak stage.

In dynamic compression tests on CTB, specimens do not fail immediately upon reaching peak stress; instead, microcracks propagate and coalesce under residual loading, resulting in continued strain accumulation amid declining overall stress. This manifests as a post-peak strain-softening regime, where stored energy dissipates through crack growth while residual stresses drive ongoing deformation, as evidenced by Zhao et al. (2024), who observed abrupt post-peak stress reduction with increasing strain in uniaxial tests, indicative of brittle failure, and Sun et al. (2021) and Guo et al. (2025), who noted energy concentration and release around cracks under impact loading, leading to internal coalescence and debris formation. For repeated-impact tests, subsequent impacts on pre-damaged specimens cause cracks to close, slide or extend under residual stresses and dynamic waves, accounting for the continuous post-peak strain rise in all curves (Tan et al., 2019). Ultimately, this post-peak strain accumulation stems from progressive damage and localized residual loading, facilitating crack propagation until complete collapse.

An intriguing phenomenon can be observed in CTB specimens: When subjected to repeated impacts at similar strain

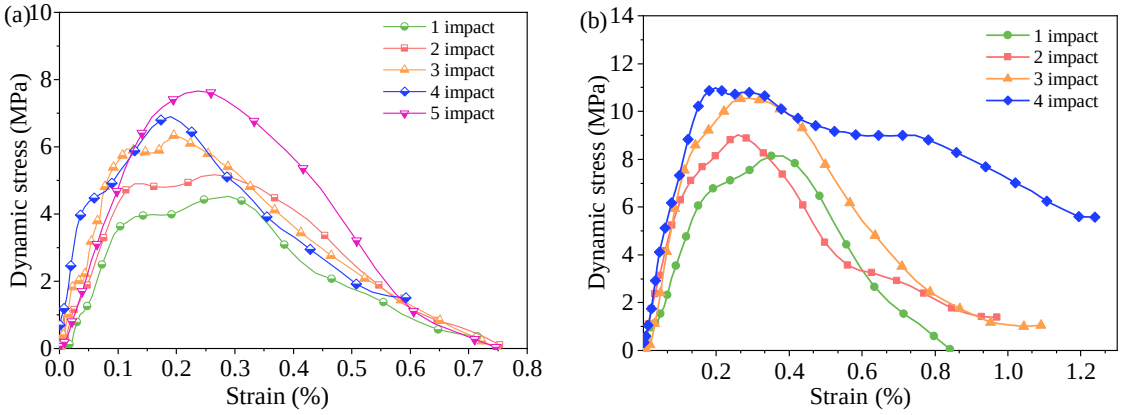

Fig. 10. Dynamic stress-strain curves of CTB under cyclic impact loading: (a) Five cycles at 52° and (b) four cycles at 61°.

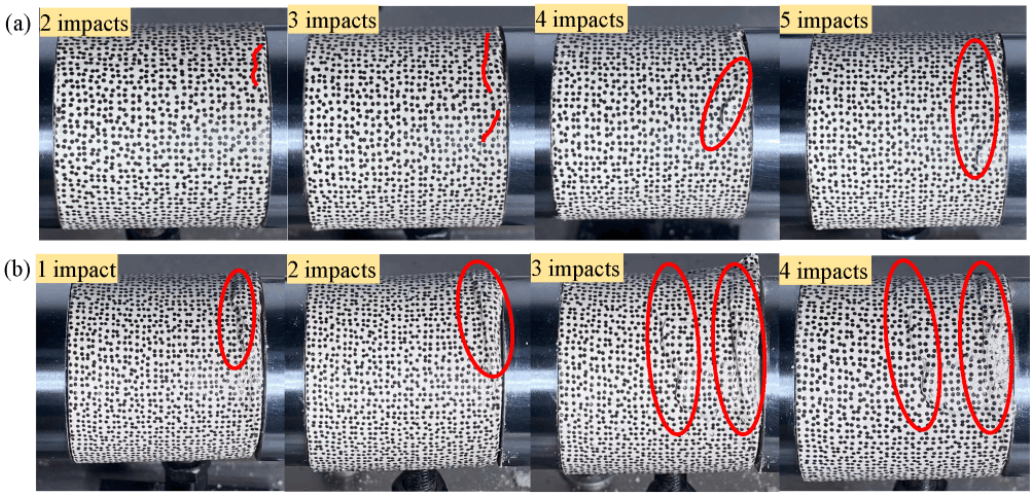

Fig. 11. Observed failure patterns of CTB specimens subjected to dynamic uniaxial cyclic impact loading: (a) With 52° impact angle and (b) with 61° impact angle.

rates without exhibiting significant damage, their peak stress incrementally increases. Specifically, following multiple impacts at a strain rate of 55 s^{-1}, the peak stresses of two CTB specimens increased from their respective initial values of 4.53 and 8.15 MPa to 7.66 and 10.98 MPa.

3.3.2 Failure pattern and DIC analysis

The CTB specimens under cyclic loading exhibits a distinctive fracture pattern. The spalling fracture pattern emerges on the side of specimens, which was firstly observed in CTB specimens. As shown in Fig. 11(a), with an increasing number of cycles, the dynamic load promotes the propagation of cracks along their existing paths, leading to the further development and interconnection of the layered cracks. Under two different impact angles, the failure modes of the specimens are similar. However, during the 61° cyclic impact, a second layered crack emerges near the midsection of specimen after the third cycle shown in Fig. 11(b), yet the specimen still maintains a certain load-bearing capacity.

A favorable explanation for this phenomenon is provided by the evolution of the strain field on the specimen surface. Fig. 12 illustrates the strain fields of the CTB specimen under the second impact, where the specimen is impacted at the velocity of 3.0 m/s. After two loading cycles, the morphology of the strain concentration area of the specimen mainly presents a grid-like distribution parallel to the impact direction. Fig. 12(b) illustrates the propagation process of the stress wave, propagating back and forth in a direction perpendicular to the axial direction.

4. Discussion

The CTB specimens tested in this work exhibited several unusual behaviors under cyclic impact loading. Within a certain range, the specimen strength rose as the impact count increased, featuring a primary damage pattern of compression-triggered plastic fractures aligned at right angles to the strike direction. This section discusses these observations and provides a rational interpretation. In addition, the effects of strain rate and impact cycles on the evolution of mechanical capacity are examined.

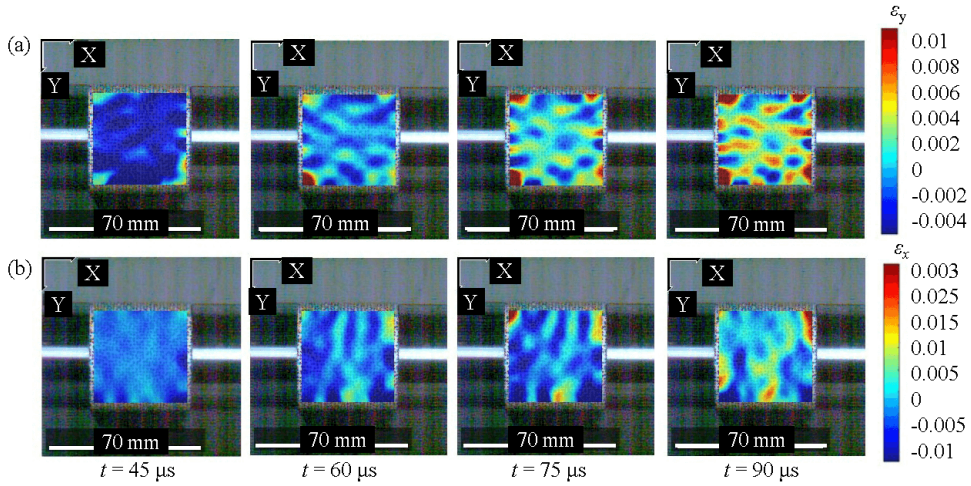

Fig. 12. DIC strain field distributions of CTB specimens during the second dynamic uniaxial cyclic impact loading at an velocity of 3.0 m/s: (a) ε_y strain field and (b) ε_x strain field.

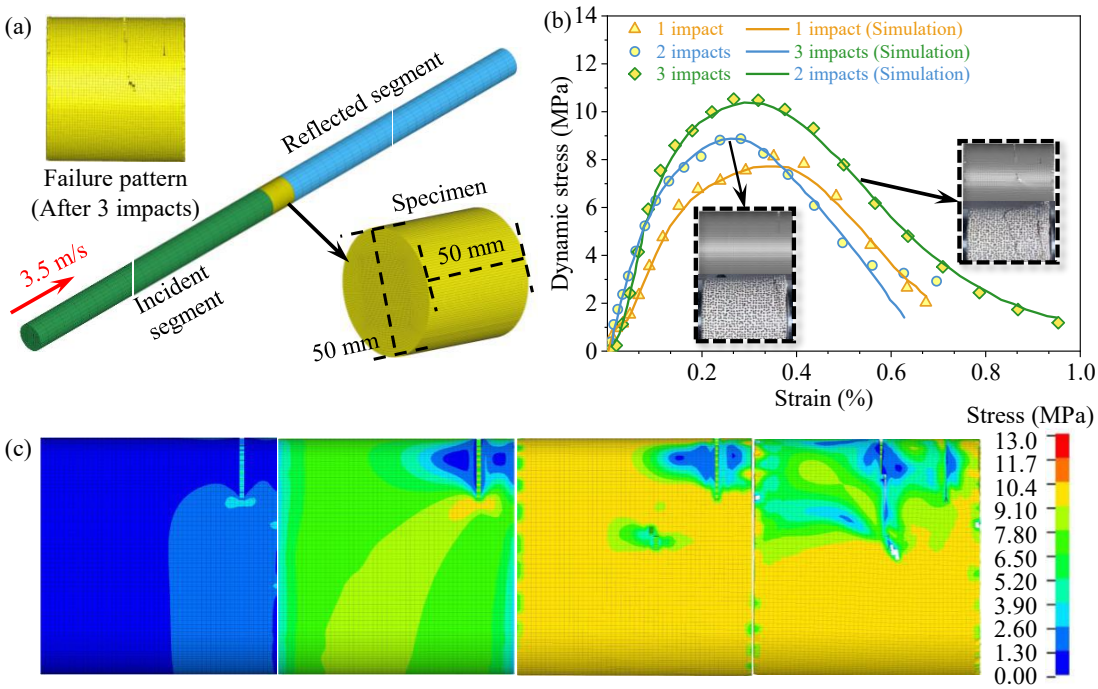

Fig. 13. Numerical simulation of SHPB response under three-cycle impacts: (a) Finite element model, (b) simulation-experiment comparison, and (c) effective von Mises stress contour at the third impact.

4.1 Fracture patterns and strength characteristics under cyclic impact

4.1.1 RHT numerical model

Numerical simulations of the CTB specimen subjected to three cyclic impacts were carried out using LS-DYNA. The corresponding numerical model was developed in strict conformity with the experimental conditions (Fig. 13(a)). The bars are composed of the same linear elastic material, while the specimen employs the RHT constitutive model. The RHT model comprises three components: A strength model, a damage model, and a porosity equation, enabling the effective description of mechanical properties and the damage evolution process (Riedel et al., 1999; Borrvall and Riedel, 2011; Heckötter and Sievers, 2017; Xu et al., 2025b). These models are used to describe failure surface, elastic-limit, linear hardening, and damage accumulation and post-failure interpolation, respectively:

$$Y_{fail}(p,\theta,\dot{\varepsilon}) = F_{fail}(p^*)R(\theta;Q_1,Q_2)\mathrm{DIF}(\dot{\varepsilon})$$
$$p^* = \frac{p}{f_c} \tag{12}$$

$$Y_{el}(p,\theta) = F_e(p^*,\theta)F_{fail}(p^*)$$

$$p_c(\alpha) = p_{comp}\left[1-\left(\frac{1-\alpha}{1-\alpha_0}\right)^{1/N}\right] + p_{el} \tag{13}$$

$$Y_y(p,\theta,\varepsilon_p,\dot{\varepsilon}) = \left[F_e(p^*,\theta) + (1-F_e(p^*,\theta))\frac{\varepsilon_p^{eff}}{\varepsilon_c^*}\right]F_{fail}(p^*)\cdot \mathrm{DIF}(\dot{\varepsilon}) \tag{14}$$

$$D(t) = \min\left(1, \frac{\sum \varepsilon_p^{eff}}{\varepsilon_f(p^*)}\right) \tag{15}$$

$$Y_d(p,\theta,D) = (1-D)F_{fail}(p^*) + DY_{fric}(p^*)$$

where $Y_{fail}(p,\theta,\dot{\varepsilon})$ refers to the failure surface phase; $F_{fail}(p^*)$ represents failure surface function as a piecewise function of normalized pressure; $R(\theta,Q_1,Q_2)$ is lode-angle correction function (Willam-Warnke type). $DIF(\dot{\varepsilon})$ is dynamic increase factor accounting for strain-rate sensitivity; p^* is normalized pressure by uniaxial compressive strength, f_c is the uniaxial compressive strength and p is surface pressure; $Y_e(p,\theta)$ refers to the elastic-limit phase; $F_e(p^*,\theta)$ is an elastic-limit factor, defined as a fraction of the failure surface along compression/tension meridians; $F_{fail}(p^*)$ is failure surface function as a piecewise function of normalized pressure; $p_c(\alpha)$ denotes to current cap pressure determined by porosity compaction (p-α model); α, α_0 is current and initial distention (ratio of porous to solid density); p_{comp} and p_{el} denote to onset and completion pressures of pore compaction, respectively; N is compaction exponent in the p-α model; $Y_y(p,\theta,\varepsilon_p,\dot{\varepsilon})$ refers to the linear hardening phase; $\varepsilon_p^e ff$ denotes accumulated effective plastic strain; ε_c^* is the reference plastic strain at which the yield surface reaches the failure surface, $\mathrm{DIF}(\dot{\varepsilon})$ is the dynamic increase factor controlled by strain rate. D represents scalar damage variable (0: Intact, 1: Fully failed); $Y_d(p,\theta,D)$ refers to the post-failure interpolation phase; $\sum \Delta\varepsilon_p^e ff$ refers to the accumulation of $\varepsilon_p^e ff$; $\varepsilon_f(p^*)$ denotes pressure-dependent failure strain controlling damage accumulation; $Y_{fric}(p^*)$ is residual frictional strength surface after complete damage.

To ensure that the RHT model accurately represents the CTB material in this study, its parameters were reidentified using the results summarized in Table 2. The calibration followed a two-phase procedure inspired by Abdel-Kader (2019). In the first phase, the basic mechanical properties were measured experimentally and subsequently used to compute all dependent and fixed parameters in the model. In the second phase, the most influential parameters were fine-tuned according to the guidance in the LS-DYNA material handbook by repeatedly running simulations and updating their values until the simulated response was consistent with the test observations.

4.1.2 Model validity and fracture pattern analysis

A mesh size of 0.1 mm ensured both satisfactory convergence and reliable crack propagation behavior. The simulated stress-strain curves showed good agreement with the experimental damage patterns (Fig. 13(b)), with relative errors in peak stress of 4.3%, 1.8%, and 2.0% for the first to third impacts, respectively. These results provide strong evidence for the validity of the model.

Under unconfined cyclic impact loading, the CTB predominantly exhibited a plastic compression failure mode oriented nearly perpendicular to the impact direction, in marked contrast to the conventional axial splitting behavior. As the impacts increased, additional circumferential cracks emerged near the specimen midsection. The distinctive pattern is attributed to the plastic properties of the CTB. Under high-velocity impact, CTB exhibited pronounced plastic behavior, with small plastic failure zones forming near the specimen ends. Upon subsequent loading, localized stress concentration zones developed around the plastic cracks (Fig. 13(c)), propagating obliquely and inducing new compressive plastic cracks in the specimen midsection. These cracks further extended and coalesced, ultimately resulting in the observed spalling fracture pattern.

Although microscopic observation was not conducted in this study, the validity of the numerical simulation is strongly supported by the DIC results. The grid-like strain concentration observed in the experiment (Fig. 12(b)) is consistent with the plastic failure zones and circumferential cracks predicted by the simulation (Fig. 13(c)). This macroscopic consistency indicates that the numerical model accurately reflects the stress evolution and failure mechanism of the CTB.

Previous studies on brittle rocks and concrete under impact loading commonly reported axial splitting or conical shear failure, which is primarily governed by tensile stress concentration along the loading direction (Li et al., 2022). In contrast, CTB exhibits higher inelastic deformability due to its heterogeneous microstructure and the presence of cementitious bonds. Recent SHPB studies on CTB have demonstrated that under high strain rates or repeated impacts, failure modes evolve from tensile and X-conjugate shear failures to crushing with finer fragmentation, driven by strain rate sensitivity, pore compaction, particle breakage, and enhanced energy dissipation (Chen et al., 2021; Song et al., 2022; Yang et al., 2025). Compared with these studies, this paper highlights a distinct spalling fracture pattern that develops progressively with increasing impact cycles. Similar circumferential or ring-shaped cracking has been reported in cemented and fiber-reinforced concrete materials under cyclic or high-energy dynamic loading, where the plastic deformation accumulated and tensile stresses exceeded bonding strength (Hamed et al., 2024; Sun et al., 2026). In our simulations, the RHT model captures this mechanism by reproducing the formation of localized plastic zones near the specimen ends during early impacts, followed by the migration of stress concentration toward the specimen midsection. This evolution is consistent with observations in the dynamic compression of cemented materials, where repeated loading leads to oblique crack growth and eventual coalescence into spalling fractures rather than axial splitting.

4.1.3 Strength characteristics of CTB

The backfill and surrounding rock jointly bear deformation loads; therefore, it is necessary to compare and analyze their strength characteristics under dynamic disturbance. Fig. 14(a) illustrates the evolution of dynamic uniaxial compressive peak stress as a function of impact cycles and its corresponding

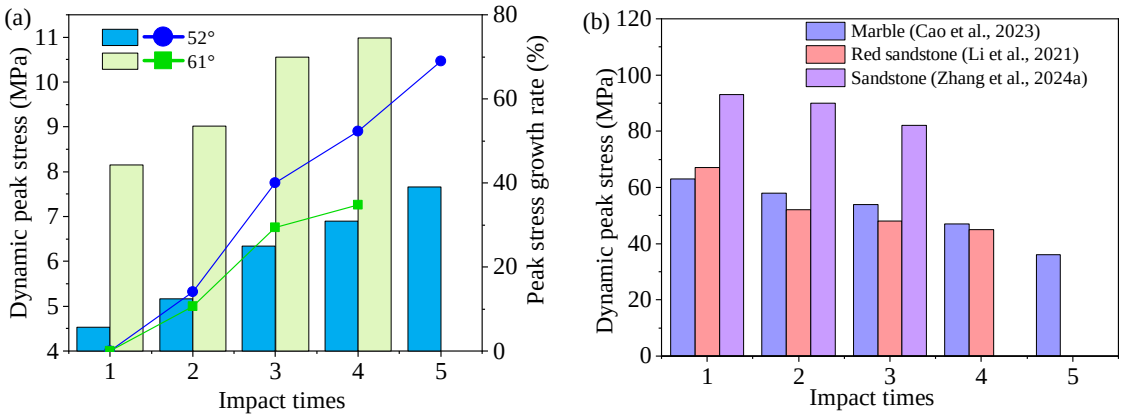

Fig. 14. Dynamic peak stress evolution with an increasing number of impact cycles: (a) CTB specimens and (b) rock specimens (Li et al., 2021; Cao et al., 2023; Zhang et al., 2024a).

growth rate. The dynamic peak compressive stress of the CTB specimens increases steadily with the number of impacts, which is likely attributed to the buildup of compressive residual stresses. Cyclic impacts may induce compressive residual stresses within the material. These residual stresses counteract external tensile stresses during subsequent impacts, delaying crack propagation and consequently contributing to an increase in peak stress. However, as presented in Fig. 14(b), unlike the CTB, dynamic cyclic loading will cause damage and failure of the rocks, leading to a decrease in peak stress and a reduction in bearing capacity. This characteristic of the filling body demonstrates a good resistance to frequent dynamic disturbances and can ensure mining safety during its service life.

4.2 Energy evolution under cyclic impact

The energy evolution process reflects the damage and failure changes in the specimen. As depicted in Fig. 15, the progression of energy in uniaxial repeated impacts may be segmented into three distinct phases, each correlating with distinct features in the stress-strain curves (Fig. 7(c)) and crack evolution (Figs. 8 and 9). In the initial stage (0-25 μs), the curves ascend gradually, signifying that most of the incident energy is accumulated in the form of elastic strain energy, aligning with the linear elastic phase in the stress-strain response where dynamic stress grows proportionally without significant microcrack initiation. During the second stage (25-120 μs), the curves rise approximately linearly due to repeated transmission and reflection of stress waves between the incident bar, CTB specimen, and transmission bar, leading to continuous energy dissipation and the propagation of both pre-existing and newly formed cracks. This corresponds to the yield phase transitioning toward peak stress, where axial microcracks begin to develop parallel to the impact direction and form vertically concentrated strain zones on the specimen surface. In the final stage (120-200 μs), the growth rate of energy gradually decreases and approaches a plateau, corresponding to the post-peak damage phase with sustained strain accumulation and plastic behavior as microcracks propagate, coalesce into a network-like structure and drive progressive deformation until eventual failure without immediate collapse.

It is worth noting that the evolution of energy and strength presents a coupled mechanism of hardening and damage. While the accumulation of compressive residual stresses enhances the bearing capacity (peak stress), the accumulated micro-damage reduces the deformation capacity of the material, leading to a synchronous decrease in its energy absorption rate.

Under dynamic loading, the energy characteristics of the specimens exhibit distinct properties. It can be observed from Figs. 15(b) and 15(c) that both the specimen energy absorption and the energy absorption rate are positively correlated with the strain rate. Specifically, higher strain rates lead to greater energy absorption, demonstrating the excellent impact resistance of CTB material under such conditions. However, the accumulated damage in the specimen expands with an increasing number of cyclic loadings. Consequently, with each successive impact, both the energy absorbed and the energy absorption rate decrease, although the specimen retains some buffering capacity.

5. Conclusions

In this paper, a comprehensive experimental program comprising dynamic tension and dynamic uniaxial compression tests (under single and cyclic impacts) was conducted to systematically evaluate the dynamic response of CTB. The results contribute to an improved understanding of the essential mechanical mechanisms and associated failure modes under diverse impact conditions. The discussion section investigates the formation mechanism of the circumferential compression plastic failure mode under cyclic loading and explains its strength characteristics, while it elucidates the effects of cyclic loading on the dynamic behavior and damage evolution of CTB. The main conclusions are summarized as follows:

1) The dynamic tensile strength of CTB specimens exhibits a positive correlation with strain rates ranging from 100 to 102 s-1. However, strain rate variations have minimal influence on the shape of tensile stress history curves. The

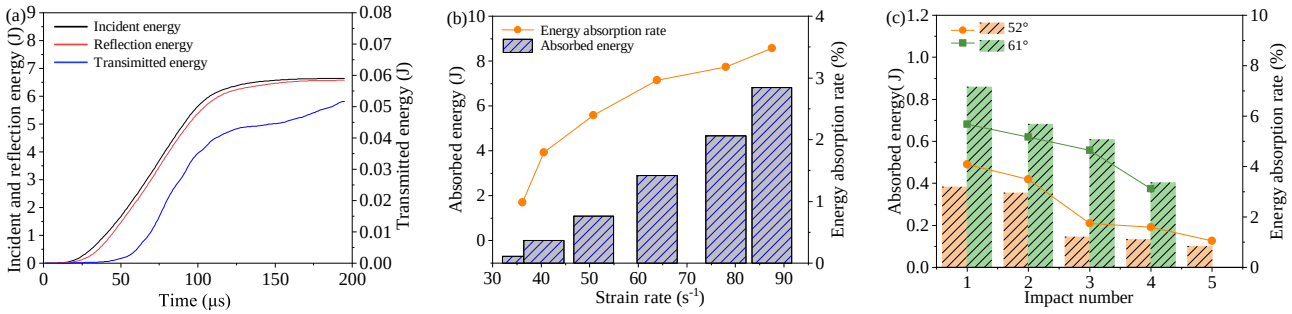

Fig. 15. Energy dissipation behavior of CTB under dynamic impact loading: (a) Uniaxial impact energy history, (b) absorbed energy and absorption rate versus strain rate, and (c) cycle number effect on energy absorption at different impact angles.

tensile crack first appears at the center of the test specimen. Failure occurs primarily through the penetration of a dominant tensile crack, splitting specimens into two roughly equal halves. Secondary cracks extend toward the boundaries, forming a shear damage zone near the contact end, the extent of which correlates with the impact rate.

2) Under dynamic uniaxial compression, the stress-strain curve of CTB is independent of the strain rate and exhibits post-peak plasticity characteristics. The dynamic compressive peak stress shows a robust linear relationship with strain rate, with DIF ranging from 1.0 to 5.3. The damage is characterized by grid-like axial microcracks that propagate across the surface, resulting in localized spalling. The damage process of CTB specimens is accompanied by energy evolution, and the stages of the energy history curve coincide with the CTB rupture process. As the strain rate increases, both energy dissipation and absorption efficiency demonstrate enhancement, reaching a peak dissipation efficiency of 8.582%. The behavior of CTB in terms of energy and deformation characteristics demonstrates its excellent load-bearing capacity under high strain rate.
3) In contrast to most rocks, dynamic cyclic loading enhances the peak stress of CTB specimens, with more pronounced increases observed at lower strain rates. The damage mode of the specimen is characterized by circumferential plastic cracks. These cracks propagate circumferentially and increase in number as the number of impacts rises. LS-DYNA finite element simulation conducted in this study revealed the formation process of plastic cracks. Cyclic loading exacerbates the damage to the specimen, resulting in a gradual decrease in both the energy absorption rate and the dissipated energy of the CTB. This finding demonstrates that the CTB samples examined in this study are capable of withstanding frequent underground dynamic load disturbances.

Acknowledgements

This study was supported by the Major National Science and Technology Project for Deep Earth of China (No. 2024ZD1003805), the National Natural Science Foundation of China (Nos. 52574100 and 52574001), and the Fundamental Research Funds for the Central Universities of China (No. FRF-IDRY-20-003). The authors gratefully acknowledge all this support.

Conflicts of interest

The authors declare no competing interest.

References

Abdel-Kader, M. Modified settings of concrete parameters in RHT model for predicting the response of concrete panels to impact. International Journal of Impact Engineering, 2019, 132: 103312.

Bieniawski, Z., Hawkes, I. Suggested methods for determining tensile strength of rock materials-1. suggested method for determining direct tensile strength. International Journal of Rock Mechanics and Mining Sciences, 1978, 15(3): 99-103.

Bischoff, P., Perry, S. Compressive behaviour of concrete at high strain rates. Materials and Structures, 1991, 24(6): 425-450.

Borrvall, T., Riedel, W. The RHT concrete model in LS-DYNA. Paper Presented at Proceedings of The 8th European LS-DYNA User Conference, Strasbourg, France, 23-24 May, 2011.

Cao, R., Wang, H., Qiu, X., et al. Damage characteristics and fracture behaviour of marble after cycle impact loading. Theoretical and Applied Fracture Mechanics, 2023, 125: 103903.

Cao, S., Yilmaz, E., Song, W. Dynamic response of cement-tailings matrix composites under SHPB compression load. Construction and Building Materials, 2018, 186: 892-903.

Chen, X., Shi, X., Zhou, J., et al. High strain rate compressive strength behavior of cemented paste backfill using split Hopkinson pressure bar. International Journal of Mining Science and Technology, 2021, 31(3): 387-399.

Cho, S., Ogata, Y., Kaneko, K. Strain-rate dependency of the dynamic tensile strength of rock. International Journal

of Rock Mechanics and Mining Sciences, 2003, 40(5): 763-777.

Deng, S., Yan, Y., Wang, X., et al. Dynamic mechanical behavior and failure characteristics of jointed rock-like specimen under impact load. Engineering Failure Analysis, 2025, 167: 108975.

Feng, X., Gong, B., Liang, Z., et al. Study of the Dynamic failure characteristics of anisotropic shales under impact brazilian splitting. Rock Mechanics and Rock Engineering, 2023, 57: 2213-2230.

Guo, J., Li, Z., Wang, X., et al. Mechanical properties and damage evolution of rock–backfill composite under impact load. Green and Smart Mining Engineering, 2025, 2(2): 109-121.

Hamed, S., Wang, S., Reg, E., et al. Pipeline circumferential cracking in near-neutral ph environment under the influence of residual stress: Dormancy and crack initiation. Metallurgical and Materials Transactions A, 2024, 55: 3640-3661.

Han, Z., Li, D., Li, X. Dynamic mechanical properties and wave propagation of composite rock-mortar specimens based on SHPB tests. International Journal of Mining Science and Technology, 2022, 32(4): 793-806.

Heckötter, C., Sievers, J. Comparison of the RHT concrete material model in LS-DYNA and ANSYS autodyn. Paper Presented at Proceedings of the 11th European LS-DYNA Conference, Salzburg, Austria, 9-11 May, 2017.

Hou, Y., Yin, S., Yang, S., et al. Mechanical properties, damage evolution and energy dissipation of cemented tailings backfill under impact loading. Journal of Building Engineering, 2023, 66: 105912.

Kolsky, H. An investigation of the mechanical properties of materials at very high rates of loading. Proceedings of the Physical Society. Section B, 1949, 62(11): 676-700.

Kolsky, H. Stress waves in solids. North Chelmsford, USA, Courier Corporation, 1963.

Li, G., Shi, X., Ning, J., et al. Particle size distribution of aggregate effects on the dynamic compressive behavior of cement waste rock backfill. Engineering Fracture Mechanics, 2023, 292: 109596.

Li, M., Hao, H., Cui, J., et al. Numerical investigation of the failure mechanism of cubic concrete specimens in SHPB tests. Defence Technology, 2022, 18(1): 1-11.

Li, S., Long, K., Zhang, Z., et al. Cracking process and energy dissipation of sandstone under repetitive impact loading with different loading rates: From micro to macro scale. Construction and Building Materials, 2021, 302: 124123.

Lifshitz, J., Leber, H. Data processing in the split Hopkinson pressure bar tests. International Journal of Impact Engineering, 1994, 15(6): 723-733.

Lin, Y., Zhou, K., Li, J., et al. Weakening laws of mechanical properties of sandstone under the effect of chemical corrosion. Rock Mechanics and Rock Engineering, 2020, 53(4): 1857-1877.

Liu, L., Li, Y., Cao, W., et al. Coupled thermo-hydro-mechanical-damage modeling of cold water injection in deep geothermal reservoirs. Journal of Rock Mechanics and Geotechnical Engineering, 2026, 18(1): 39-54.

Liu, K., Zhang, Q., Wu, G., et al. Dynamic mechanical and fracture behaviour of sandstone under multiaxial loads using a triaxial hopkinson bar. Rock Mechanics and Rock Engineering, 2019, 52(7): 2175-2195.

Liu, K., Zou, C., Zhao, J. Dynamic tensile behaviour of rocks under confining pressure and high-rate loadings. Earth Energy Science, 2025a, 1(1): 9-21.

Liu, L., Ji, H., Elsworth, D., et al. Dual-damage constitutive model to define thermal damage in rock. International Journal of Rock Mechanics and Mining Sciences, 2020, 126: 104185.

Liu, L., Zhang, Z., Wang, T., et al. Evolution characteristics of fracture volume and acoustic emission entropy of monzogranite under cyclic loading. Geomechanics and Geophysics for Geo-Energy and Geo-Resources, 2024, 10(1): 16.

Liu, L., Jin, J., Liu, J., et al. Mechanical properties of sandstone under in-situ high-temperature and confinement conditions. International journal of minerals metallurgy and materials, 2025b, 32(4): 778-787.

Malik, A., Chakraborty, T., Rao, K. Strain rate effect on the mechanical behavior of basalt: Observations from static and dynamic tests. Thin-Walled Structures, 2018, 126: 127-137.

Qu, H., Liu, L., Suo, Y., et al. Anisotropic characteristics of layered backfill: Mechanical properties and energy dissipation. Journal of Rock Mechanics and Geotechnical Engineering, 2023, 15(12): 3188-3208.

Riedel, W., Thoma, K., Hiermaier, S., et al. Penetration of reinforced concrete by Beta-B-500 numerical analysis using a new macroscopic concrete model for hydrocodes. Paper Presented at Proceedings of the 9th International Symposium on the Effects of Munitions with Structures, Berlin, Germany, 3-7 May, 1999.

Song, C., Lu, C., Liu, H., et al. Moment tensor and stress field inversions of mining-induced seismicity in a thick-hard roof zone. Rock Mechanics and Rock Engineering, 2024, 57(3): 2267-2287.

Song, X., Hao, Y., Wang, S., et al. Dynamic mechanical response and damage evolution of cemented tailings backfill with alkalized rice straw under SHPB cycle impact load. Construction and Building Materials, 2022, 327: 127009.

Sun, B., Liu, S., Zeng, S., et al. Dynamic characteristics and fractal representations of crack propagation of rock with different fissures under multiple impact loadings. Scientific Reports, 2021, 33: 13071.

Sun, R., Huang, D., Yao, X., et al. Effect of dynamic expansion of interface micro-annulus on casing failure mechanism during multistage fracturing. Geoenergy Science and Engineering, 2026, 257: 214227.

Tan, Y., Davide, E., Zhou, Y., et al. Long-term mechanical behavior and characteristics of cemented tailings backfill through impact loading. International Journal of Minerals, Metallurgy, and Materials, 2020, 27(2): 140-151.

Tan, Y., Yu, X., Elmo, D., et al. Experimental study on dynamic mechanical property of cemented tailings backfill under SHPB impact loading. International Journal of

Minerals, Metallurgy, and Materials, 2019, 26(4): 404-416.

Wang, A., Cao, S., Yilmaz, E. Effect of height to diameter ratio on dynamic characteristics of cemented tailings backfills with fiber reinforcement through impact loading. Construction and Building Materials, 2022, 322: 126448.

Wang, B., Yang, L., Li, Q., et al. Mechanical behavior, acoustic emission and principal strain field evolution properties of layered cemented paste backfill under unconfined compression. Construction and Building Materials, 2024a, 415: 135111.

Wang, T., Ye, W., Liu, L., et al. Disturbance failure mechanism of highly stressed rock in deep excavation: Current status and prospects. International Journal of Minerals, Metallurgy and Materials, 2024b, 31(4): 611-627.

Wang, T., Ye, W., Liu, L., et al. Denoising of acoustic emission signals from rock failure processes through ICEEMDAN combined with multiple criteria and wavelet transform. Discover Applied Sciences, 2025a, 7(4): 255.

Wang, D., Dong, Y., Wei, C., et al. Expansion-induced fracture propagation in deep geothermal reservoirs under alternate-temperature loading. Advances in Geo-Energy Research, 2025b, 15(3): 261-272.

Xu, Z., Wu, C., Yu, M., et al. Static mechanical properties of rock-concrete composite specimens after high-temperature treatment. Rock Mechanics and Rock Engineering, 2025a, 58: 13741-13765.

Xu, Z., Wu, C., Yu, M., et al. Dynamic compressive behavior and energy absorption of SFRC. Journal of Building Engineering, 2025b, 106: 112554.

Xue, G., Yilmaz, E., Feng, G., et al. Reinforcement effect of polypropylene fiber on dynamic properties of cemented tailings backfill under SHPB impact loading. Construction and Building Materials, 2021, 279: 122417.

Yang, L., Liu, Z., Sun, Q., et al. Mechanical properties, failure modes, energy consumption characteristics and damage constitutive model of early damaged cemented tailings backfill under impact loading. Structures, 2025, 82: 110725.

Yao, W., He, T., Xia, K. Dynamic mechanical behaviors of Fangshan marble. Journal of Rock Mechanics and Geotechnical Engineering, 2017, 9(5): 807-817.

Zhang, L., Wang, E., Liu, Y., et al. Experimental research into the dynamic damage characteristics and failure behavior of rock subjected to incremental repeated impact loads. Engineering Geology, 2024a, 331: 107435.

Zhang, S., Sun, W., Hou, Z., et al. Research on damage and crack evolution mechanism of backfill under the coupling effect of layer-inclined angle-pore triple defect structure. Construction and Building Materials, 2024b, 444: 137793.

Zhao, K., Ma, C., Yang, J., et al. Pore fractal characteristics of fiber-reinforced backfill based on nuclear magnetic resonance. Powder Technology, 2023, 426: 118678.

Zhao, Z., Yang, J., Kang, Y., et al. Microcrack monitoring and fracture evolution of coal and rock using integrated acoustic emission and digital image correlation techniques. Scientific Reports, 2024, 14: 8063.

Zheng, D., Song, W., Cao, S., et al. Investigation on dynamical mechanics, energy dissipation, and microstructural characteristics of cemented tailings backfill under shpb tests. Minerals, 2021, 11(5): 542.

Zhu, D., Huang, N., Xiao, Q., et al. Enhancing dynamic mechanical properties of cemented lithium mica tailings backfill with alkaline rice straw fibers: Experimental investigation and microscopic analysis. Developments in the Built Environment, 2024, 20: 100563.

Zhu, G., Zhu, W., Qi, Z., et al. One-part alkali-activated slag binder for cemented fine tailings backfill: Proportion optimization and properties evaluation. Environmental Science and Pollution Research, 2022, 29(49): 73865-73877.

Zhu, T., Chen, Z., Cao, J., et al. Crack resistance of cemented waste rock tailings backfill under splitting tensile load: Experimental and numerical investigations. Journal of Building Engineering, 2025, 99: 111665.

Zou, S., Gao, Y., Zhou, Y., et al. Study on the multi-scale tensile mechanical behavior of fiber reinforced cemented tailings backfill considering surface roughness effects. Construction and Building Materials, 2025a, 462: 139988.

Zou, S., Gao, Y., Zhou, Y., et al. Mechanical properties of organic-inorganic hybrid fiber reinforced cemented tailings backfill considering energy evolution and damage fracture characteristics. Journal of Materials Research and Technology, 2025b, 35: 4614-4633.